

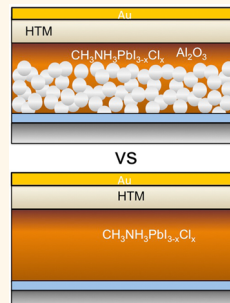
Electronic Properties of Meso-Superstructured and Planar Organometal Halide Perovskite Films: Charge Trapping, Photodoping, and Carrier Mobility

Tomas Leijtens,[†] Samuel D. Stranks,[†] Giles E. Eperon,[†] Rebecka Lindblad,[‡] Erik M. J. Johansson,[§] Ian J. McPherson,^{||} Håkan Rensmo,[‡] James M. Ball,[†] Michael M. Lee,[†] and Henry J. Snaith*,[†]

[†]University of Oxford, Clarendon Laboratory, Parks Road, Oxford OX1 3PU, U.K., [‡] Department of Physics and Astronomy, Molecular and Condensed Matter Physics, Uppsala University, Box 516, SE 751 20 Uppsala, Sweden, [§]Department of Chemistry-Ångström, Uppsala University, Box 523, SE 751 20 Uppsala, Sweden, and

^{||}Inorganic Chemistry Laboratory, Department of Chemistry, University of Oxford, South Parks Road, Oxford OX1 3QR, U.K.

ABSTRACT Solution-processed organometal trihalide perovskite solar cells are attracting increasing interest, leading to high performances over 15% in thin film architectures. Here, we probe the presence of sub gap states in both solid and mesosuperstructured perovskite films and determine that they strongly influence the photoconductivity response and splitting of the quasi-Fermi levels in films and solar cells. We find that while the planar perovskite films are superior to the mesosuperstructured films in terms of charge carrier mobility (in excess of $20 \text{ cm}^2 \text{ V}^{-1} \text{ s}^{-1}$) and emissivity, the planar heterojunction solar cells are limited in photovoltage by the presence of sub gap states and low intrinsic doping densities.



KEYWORDS: perovskite · solar cells · mobility · traps · doping

Solid-state hybrid solar cells made with methylammonium lead trihalide perovskites have rapidly improved in performance from around 10%^{1,2} to over 15%^{3,4} power conversion efficiency (PCE) over an 18 month period. Methylammonium lead triiodide, $\text{CH}_3\text{NH}_3\text{PbI}_3$, and a “mixed halide” variant prepared from PbCl_2 and methylammonium, $\text{CH}_3\text{NH}_3\text{PbI}_{3-x}\text{Cl}_x$, are the perovskite absorbers that have been the subject of the most intense interest. While both were initially used as traditional light absorbing sensitizers on a mesoporous TiO_2 scaffold, along with an organic hole transporter 2,2',7,7'-tetrakis(*N,N*-di-*p*-methoxyphenylamine)9,9'-spirobifluorene (spiro-MeOTAD),^{1,2} the materials are capable of both strong light extinction and efficient transport of photogenerated species. Lee *et al.* demonstrated that the “mixed halide” perovskite was capable of transporting electrons when coated onto an insulating alumina (Al_2O_3) scaffold in an architecture

now termed mesosuperstructured solar cells (MSSCs)¹ and also showed operation of planar heterojunction perovskite solar cells, where the perovskite assumes the roles of light absorption as well as transport of photogenerated species, albeit initially at much lower efficiencies. Etgar *et al.* showed that $\text{CH}_3\text{NH}_3\text{PbI}_3$ was capable of transporting holes when the perovskite was completely infiltrated into a TiO_2 scaffold.^{5,6} Ball *et al.* subsequently showed that the mixed halide perovskite is capable of functioning in a thin film planar heterojunction solar cell configuration with an exceptional internal quantum efficiency (IQE) approaching 100%.⁷ Several recent reports have found the photogenerated carrier diffusion lengths to be on the order of $1 \mu\text{m}$,^{8–11} while Stranks *et al.* and Deschler *et al.* have demonstrated high photoluminescence quantum efficiencies (PLQE) in neat perovskite films (albeit only at high excitation densities where all traps states have been filled), confirming that

* Address correspondence to h.snaith1@physics.ox.ac.uk.

Received for review April 16, 2014 and accepted June 20, 2014.

Published online June 20, 2014
10.1021/nn502115k

© 2014 American Chemical Society

such planar heterojunction solar cells have the potential to reach very high photovoltage and efficiency.^{12,13} Indeed, planar heterojunction solar cells of very good efficiency have been reported in many different configurations.^{8,14–16} However, the most efficient architecture in the report by Ball *et al.* was one where a low-temperature-processed mesoporous Al_2O_3 scaffold was completely infiltrated with the perovskite, postulated to aid film formation, raising photovoltages and fill factors, but decreasing the IQE.⁷ This meso-superstructure has led to performances of close to 16% with further optimization, specifically by introducing an additional perovskite capping layer on top of the infiltrated mesoporous scaffold.^{17,18} If the only role of the mesoporous Al_2O_3 is to assist film formation, it should then appear to be superfluous with optimal perovskite processing conditions. Still, despite improvements in film formation enabling uniformly coated planar heterojunction perovskite solar cells,^{3,16,19,20} there are as yet no examples of solution-processed planar heterojunction solar cells delivering open circuit voltages approaching those found in MSSCs, limiting the obtainable power conversion efficiency. The highest open-circuit voltages attained in solution-processed planar heterojunctions are around 1 V,^{3,16,19,20} whereas MSSCs have achieved greater than 1.1 V.¹ We note, however, that high open circuit voltages have been observed for evaporated planar heterojunction solar cells,³ but this may be due to smaller crystal sizes present in the evaporated films as well as differences in crystal formation,^{3,7,19} the effects of which will be discussed later on.

Here, we explore charge carrier trapping, transport, and emission in solution-processed $\text{CH}_3\text{NH}_3\text{PbI}_{3-x}\text{Cl}_x$ films in the planar heterojunction (solid) and mesosuperstructured architectures. Through photoelectron spectroscopy we find evidence for a large density of sub gap electronic trap sites, whose distribution and occupancy is heavily influenced by the Al_2O_3 scaffold. We postulate that long-lived electron trapping in such sites leads to an accumulation of free holes in both architectures under illumination (photodoping). This large hole density dominates the photoconductivity under solar illumination light levels. Moreover, the mesoporous Al_2O_3 scaffold raises the Fermi level of the perovskite, either due to surface states such as under-coordinated halides acting as shallow donors, or due to an electro-static interaction between the oxide and the perovskite. While we demonstrate that the photoluminescence quantum efficiency (PLQE) and long-range charge transport are superior in solid perovskite films, the solar cells suffer from reduced photovoltages and fill factors even after optimization of film morphology. We propose that the high density of sub gap states limits photovoltages of the planar heterojunction solar cells, and we propose possible avenues to solve this problem.

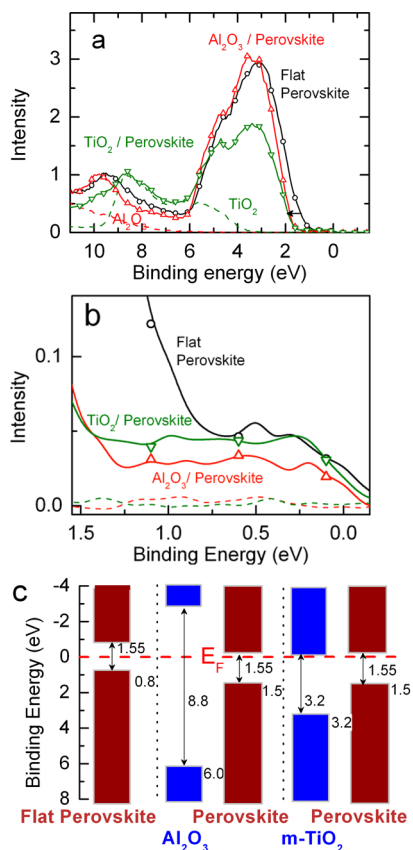


Figure 1. (a) HAXPES spectra measured with a photon energy of 3993 eV. The valence band for a flat perovskite film on glass (black circles), perovskite infiltrated into mesoporous TiO_2 (green inverted triangles) and Al_2O_3 (red triangles), and mesoporous TiO_2 (green dotted lines) and Al_2O_3 (red dotted line) without perovskite. (b) Close-up of (a) in the sub gap region below the Fermi level. (c) Conduction and valence bands are displayed relative to the Fermi level for the different materials used. We note that the positions for mesoporous (m) TiO_2 and Al_2O_3 come from the samples without perovskite.

RESULTS AND DISCUSSION

To understand the electronic alignment and determine the Fermi level of the perovskite material in different device architectures, we performed hard X-ray photoelectron spectroscopy (HAXPES) on flat, mesoporous TiO_2 , and mesoporous Al_2O_3 perovskite architectures.²¹ We ensured that there were only very thin perovskite capping layers in the mesoporous architectures, so that the surface represents the electronic structure of the perovskite infiltrated into the mesoporous scaffold. In Figure 1a we plot the HAXPES spectra, where we have set the Fermi level to be at 0 eV. The position of the perovskite Fermi level with respect to the conduction and valence bands is depicted in Figure 1c, and we give a full description of how this is done in the Supporting Information as well as a demonstration that the measurement does not degrade the samples (Figure S1, Supporting Information). Both the mesoporous TiO_2 and Al_2O_3 scaffolds appear to raise the Fermi level of the perovskite to just below (~ 50 meV)

the conduction band, while the neat solid perovskite film on fluorine-doped tin oxide (FTO) glass appears to have the Fermi level near the middle of the band gap. We, moreover, observe a significant population of midgap states filled up to the Fermi level in all the structures presented (Figure 1b). Such an effect has recently been observed in mesoporous TiO_2 -based perovskite samples and was ascribed to the sub gap states of the mesoporous TiO_2 .²¹ Since we observe these states in the perovskite in both the mesoporous TiO_2 -free planar and mesoporous Al_2O_3 architectures, these states must correspond mainly to filled sub gap states in the perovskite material itself. Similar band gap states were also observed in $\text{CH}_3\text{NH}_3\text{PbI}_3$ perovskite samples in mesoporous TiO_2 , and one reason for the bandgap states may be the small amounts of metallic Pb also observed in these perovskites.²¹ The presence of sub gap states, approximately uniformly distributed throughout the gap, has also recently been observed in the form of a capacitance in solar cells composed of these materials as well as from theoretical calculations of the material's density of states, specifically iodide vacancies taking the form of Pb^{1+} and Pb^{2+} defects.^{22,23} In fact, electron paramagnetic resonance (EPR) studies have demonstrated that Pb^{2+} can trap electrons in organic–inorganic lead halide perovskites to form paramagnetic Pb^0 clusters, very consistent with our observation of the sub gap HAXPES absorption.²⁴

We also performed cyclic voltammetry on flat perovskite films and those infiltrated into mesoporous Al_2O_3 , which we show in Figure S2 (Supporting Information). The electrolyte was composed of chlorobenzene and an inert salt, which did not change the absorption spectrum of the films even during the measurement. By following a protocol introduced by Bertoluzzi *et al.*,²⁵ we confirm the presence of electron-accepting sub gap states in both architectures. Again, we observe that these states are predominantly filled in the meso-superstructured films, while the solid planar films exhibit a large availability of empty trap sites, confirming the HAXPES results. We also point out that if electron trapping is occurring via Pb^{2+} (iodide vacancies) reduction, then the filled trapped state should be very stable and long-lived.

One key difference between the solid and meso-superstructured perovskite films is that the crystal grain size differs from greater than 500 nm to approximately 60 nm, respectively.^{7,19} From the HAXPES measurements above, the density of mid gap states in the two configurations appears to be approximately the same, at least at energies below the Fermi level of the neat perovskite film. However, the sub gap states in the meso-superstructured films are predominantly filled, whereas those in the solid films are empty from the middle of the gap. A large density of sub gap states, and the degree to which they are filled, should have an influence on long-range charge carrier transport. In

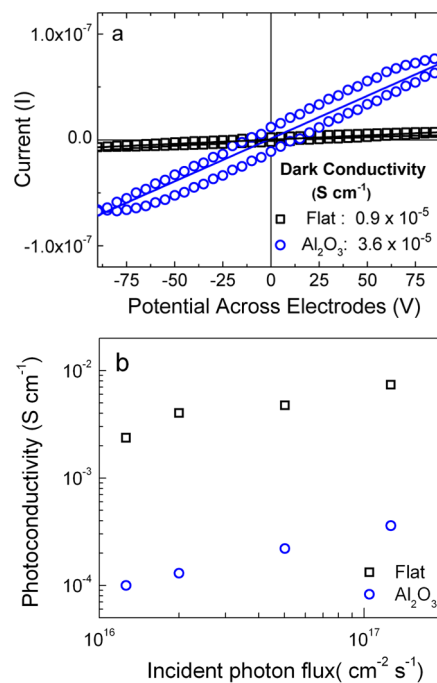


Figure 2. (a) Current–voltage curves for flat and Al_2O_3 -structured perovskite films obtained by four-point probe measurements in the dark. The inset gives the extracted conductivity. (b) Photoconductivities of the same samples under a range of continuous-wave (CW) 473 nm excitation densities, where $10^{17} \text{ cm}^{-2} \text{ s}^{-1}$ corresponds approximately to the absorbed photon flux for the material under AM1.5 100 mW cm^{-2} sunlight between 400 and 800 nm wavelength.

order to probe this, we performed four-point probe conductivity measurements in the dark (Figure 2a) and under steady-state photoexcitation by a 473 nm laser source (Figure 2b). The samples were composed of perovskite films with and without an Al_2O_3 scaffold, with gold electrodes deposited directly on top in an in-plane configuration such that we measured the lateral conductivity.^{26,27} A 200 nm layer of PMMA was deposited on top of the finished samples to protect them from the atmosphere. In calculating the *effective* conductivity, we use the whole cross-sectional area of the film, so it is not corrected for fractional volume of the perovskite when we use the mesoporous scaffold. We also note that the samples were prepared such that there is no continuous capping layer over the mesoporous Al_2O_3 , but the pores are predominantly filled (as described in the Materials and Methods), ensuring that our conductivity measurements accurately reflect the properties of the perovskite material inside the mesoporous structure. The same structures were used for all conductivity measurements in this work. As we show in Figure 2a, the effective dark conductivity of the Al_2O_3 -structured perovskite films is 4-fold higher than that in the flat films, which is counterintuitive when the film architectures are considered: the flat films have a larger volumetric fraction of perovskite, should offer a less tortuous path for electron conduction, and are composed of much larger crystals.^{7,19} However,

considering the HAXPES measurements, we expect the Fermi level to be much closer to the conduction band for the meso-superstructured perovskite films, and hence, the density of free carriers in the dark should be much higher than in the solid flat films. Upon photogeneration of free carriers, the flat samples reach extremely high photoconductivities of close to $10^{-2} \text{ S cm}^{-1}$ at photoexcitation density of $10^{17} \text{ photons cm}^{-2} \text{ s}^{-1}$ (approximately the same absorbed photon flux as under full sun illumination),²⁸ while that for the meso-superstructured samples does not surpass $5 \times 10^{-4} \text{ S cm}^{-1}$.

The high photoconductivity reached under equivalent solar fluxes provides direct evidence for a long-lived free charge population in both types of architectures, although the meso-superstructured samples must have lower mobilities and/or steady-state charge densities as evidenced by their lower photoconductivities. We note that both structures exhibit optical densities of over 1 at the excitation wavelength (Figure S3, Supporting Information), such that the large differences in photoconductivity are not expected to come from differences in light absorption. Recent work²⁸ has demonstrated that an equilibrium exists between free charge carriers and excitonic species under illumination. This equilibrium shifts toward increasing exciton population at high photoexcitation densities but is dominated by free charges at solar fluxes ($10^{17} \text{ cm}^{-2} \text{ s}^{-1}$), consistent with the high photoconductivities observed at our excitation fluxes.

We have recently developed a model that describes the influence of sub gap states on the dynamics of photogenerated species in perovskite films.¹³ We proposed that under low illumination intensities, similar to solar irradiation, photoexcited electrons are trapped with slow ($\mu\text{s-ms}$) trap filling and emptying time scales. For every trapped electron, there is one photogenerated hole with a lifetime at least as long as the trapped electron's lifetime, so a very high population of photoexcited (photodoped) holes can accumulate in the material, as we depict in Figure 3a. It should be noted that if the trap states are partially positively charged (as they would be in the case of iodide vacancies), the filled trap sites would be expected to be quite long-lived.

To study these phenomena, we performed the photoconductivity measurements under modulated continuous laser light at 473 nm and monitored the conductivity as a function of time. We should observe a large decrease in the steady-state photoconductivity if we remove the holes from the perovskite layer by using the hole-quenching material spiro-MeOTAD instead of the electronically inert PMMA to coat the perovskite films. Spiro-MeOTAD is not sufficiently conductive to affect the measured photoconductivities but will nevertheless rapidly remove holes from the perovskite as we have previously demonstrated on similar samples by photoluminescence quenching studies.^{8,27,29} In the absence of electron trapping, one would expect to observe higher photoconductivities for such samples

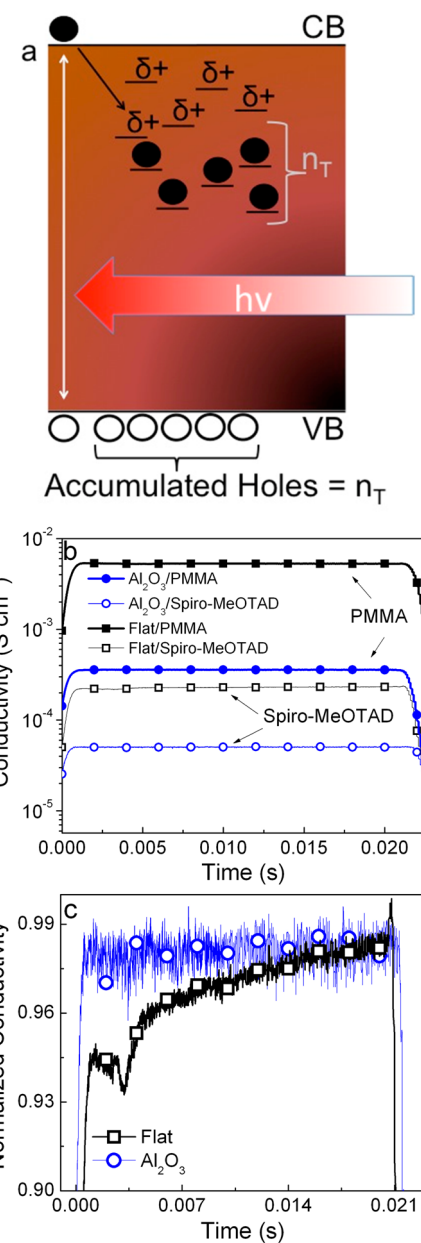


Figure 3. (a) Schematic demonstrating how after photoexcitation, n_T electrons can be trapped in an arbitrary density of trap sites, giving rise to an equal density of long-lived free holes, which will dominate the conductivity response. (b) Photoconductivity of solid (black squares) and meso-superstructured (blue circles) perovskite films with PMMA (closed symbols) and spiro-MeOTAD (open symbols) layers on top. (c) Early time rise in normalized photoconductivity of solid (black closed squares) and meso-superstructured (blue closed circles) perovskite films with spiro-MeOTAD layers on top. The strange shape in the first 5 ms of the flat perovskite sample is an instrument artifact due to an error in the trigger of the oscilloscope. A 473 nm laser source was used at an excitation density of $1.2 \times 10^{17} \text{ cm}^{-2} \text{ s}^{-1}$ (taking optical density of the samples into account) and chopped at 23 Hz to verify that the high conductivity is photoinduced.

as long-lived charge separation (holes in the spiro-MeOTAD) means that the electron population in the perovskite should be much enhanced. However, we observe the contrary. In Figure 3b, we observe that the

photoconductivities (the flat section of the curves corresponding to the time of the laser exposure) of both flat and meso-superstructured samples with spiro-MeOTAD are approximately factors of 30 and 10 lower, respectively, than when PMMA is used. This is consistent with the photoconductivity in the films coated with the inert PMMA being dominated by electron trapping and associated hole accumulation.

In Figure 3c, we normalize the conductivity traces and compare the photoconductivity as a function of time for the flat and Al_2O_3 -structured samples coated with the spiro-MeOTAD hole collection layer. We find that the flat samples exhibit a slow rise in photoconductivity (ignoring the dip in the first 5 ms which is an instrument artifact). We have already observed that electron trapping dominates under these illumination conditions, and the photoconductivity here is unlikely to be dominated by accumulated holes since these will transfer to the spiro-MeOTAD layer. We then postulate that the observed rise corresponds to a trap filling time. As more traps are filled, relatively more photoexcited electrons remain in the conduction band to contribute to the observed photoconductivity. The rise time is very slow, on the order of 20 ms, indicative of a high density of sub bandgap states. For the films infiltrating mesoporous Al_2O_3 , the maximum is already reached within the time response of our instrument. This is consistent with the traps already being predominantly filled in these samples, as evidenced by the higher Fermi level in the dark determined from the HAXPES measurements.

The remaining difference in absolute magnitudes (Figure 4b) for these samples must then be the result of either shorter lifetimes or lower mobilities of free electrons within the meso-superstructured films. We note that since the fluences used for these steady-state measurements were relatively low, at $10^{17} \text{ cm}^{-2} \text{ s}^{-1}$, we do not expect the photoconductivities in this set of measurements to be affected by a changing proportion of excitons (which will not contribute to conductivity) compared to free charges.²⁸

The difference in steady-state photoconductivity could stem from either lower mobilities or lower lifetimes of free carriers. In order to distinguish these possibilities, we have performed transient conductivity measurements on similar samples. Here, we take the same device architectures and measurement setup as was used for the modulated continuous wave laser beam experiment but now use a 5 ns laser pulse as the excitation source. Since lifetimes for photogenerated species have already been shown to be on the order of 10–100s of nanoseconds at low fluences for both architectures, we do not expect a significant fraction of the excited carriers to recombine in the first 5 ns.^{8,11} We can then compare the initial increase in conductivity upon excitation with the excitation density (using the optical density of the samples and carefully measured pump power) to estimate mobilities of our samples

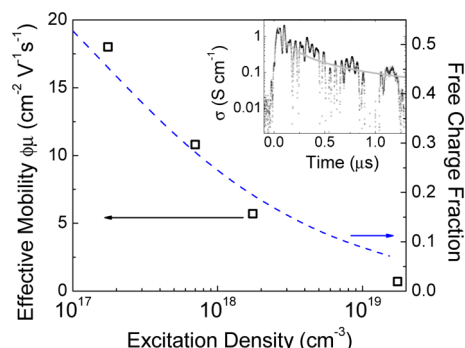


Figure 4. Effective mobility ($\phi\mu$), where $0 < \phi > 1$, values estimated from the initial value of the photoinduced conductivity perturbation upon 5 ns laser excitation at 500 nm for flat perovskite samples of the same architecture as those used for the steady-state photoconductivities. The right axis gives the fraction of the photoexcited species that are predicted to be in the form of free charges rather than excitons at a given excitation density, derived from our recent model.¹³ The inset gives an example (at excitation density of $1.7 \times 10^{18} \text{ cm}^{-3}$) of the transient conductivity traces used to determine the effective mobilities. The FCF is derived from our recently developed model for the photo-generated species.¹³ ϕ can be approximated by $2 \times \text{FCF}$ (assuming equal electron and hole mobilities) to give absolute mobilities around $20 \text{ cm}^2 \text{ V}^{-1} \text{ s}^{-1}$.¹¹

at a range of different excitation densities. This is analogous to the method used to obtain mobility from time-resolved terahertz (THz) photoconductivity measurements,¹¹ but at later times and employing electronic contacts. In Figure 4, we plot the estimated effective mobilities for flat perovskite films as a function of excitation density, along with an estimation of the fraction of the total photoexcitations that exist as free charges based on our recently developed model.¹³ The inset gives an example of the conductivity traces used to estimate the effective mobilities. We note that the decay appears to be on a similar time scale to what has been previously observed for photoluminescence and microwave decays for similar samples,³⁰ but a full analysis of the decays is beyond the scope of this work, where we merely use the initial amplitude of the perturbation to estimate effective mobilities. The effective mobility ($\phi\mu$) is calculated by the simple relations

$$\sigma = eI_{\text{ABS}}\phi\mu \quad (1)$$

$$\phi\mu = \phi(\mu_n + \mu_p) \quad (2)$$

where σ is the conductivity, e the elemental charge, I_{ABS} the absorbed excitation density as determined from the laser pulse intensity and the absorbance of the films (Figure S3), ϕ the free charge fraction of I_{ABS} , and μ the combined mobility of electrons (μ_n) and holes (μ_p). Here, we observe that the effective mobility appears to decrease with excitation density, and this is consistent with the branching ratio between free charges and excitons reducing with increasing excitation density and hence ϕ reducing correspondingly.²⁸ We confirm this by plotting the free charge fraction on the right-hand axis and see that the effective mobility follows

the free charge fraction closely. We could not perform measurements at lower fluences because the photo-induced change in photoconductivity was below our resolution. To obtain approximations for absolute mobilities, we simply assume that ϕ is the calculated branching ration between free charges and excitations for a material with an exciton binding energy of 50 meV,²⁸ which gives long-range combined lateral mobilities (μ) of around $40 \text{ cm}^2 \text{ V}^{-1} \text{ s}^{-1}$ within our range of excitation densities. Since the electron and hole masses for the material have been predicted to be approximately equal,^{31,32} the single carrier mobility becomes $20 \text{ cm}^2 \text{ V}^{-1} \text{ s}^{-1}$. This corresponds well to recently reported values for single-crystal mobilities measured by the hall effect in the dark as well as THz measurements of similar films.^{30,33} We also note that this is one of the highest reported long-range mobilities for solution-processed semiconductors, placing the material among the highest quality organic or metal oxide semiconductors for use in a variety of semiconducting devices.^{34,35}

The photoinduced increase in conductivity for meso-superstructured samples was not large enough to resolve on our experimental setup at any of the excitation densities attempted, despite the fact that the free carrier decay rates ($0.01\text{--}0.1 \text{ ns}^{-1}$) have been shown to be slow enough that we should be able to resolve it temporally, at least at the lower fluences used.¹¹ This, together with the steady-state photoconductivity data, suggests that the mobility of photogenerated carriers within the perovskite infiltrated into the mesoporous network is more than 1 order of magnitude lower than the mobility in the flat solid films.

We note that Wehrenfennig *et al.*¹¹ have recently reported mobilities of $10 \text{ cm}^2 \text{ V}^{-1} \text{ s}^{-1}$ for meso-superstructured perovskite films using time-resolved terahertz spectroscopy. Terahertz mobilities are local (likely single crystal) mobilities which should correspond more closely to what we have measured for the flat perovskite films. Here, we are probing the long-range (1 cm) effective mobility over which distance the charges have a far greater probability of becoming trapped or scattered at grain boundaries and defects and have to traverse tortuous pathways through the mesoporous framework and numerous crystal boundaries. Such discrepancies between THz and long-range mobility have also been previously observed for nanostructured metal oxide semiconductors such as TiO_2 and SnO_2 .^{27,36} We note that the perovskite crystal grain size within the mesoporous scaffold is on the order to 60 nm, whereas it is greater than 100+ nm (and likely on the order of microns) in the flat solid films.⁷ Notably, the similarity between the THz mobility and the long-range mobility extracted here suggests that in the solid thin films grain boundaries pose little inhibition to long-range charge transport, consistent with negligible potential barrier present at the grain boundaries.³⁷

TABLE 1. Performance Parameters of the Current–Density vs Voltage Curves Presented in Figure 5.^a

	J_{sc} (mA cm^{-2})	PCE (%)	V_{oc} (V)	FF	PLQE (%)
Al_2O_3	16.7	10.6	1.00	0.63	20.3 ± 0.05
Flat	16.8	9.4	0.88	0.64	19.1 ± 1.3

^a Statistics for a batch of over 15 devices for each architecture are given in Figure S3 (Supporting Information).

This low long-range mobility makes the relatively high (compared to the solid perovskite) dark conductivity of the Al_2O_3 -structured samples (from Figure 2a) especially noteworthy. However, considering the HAXPES results, the high Fermi level in these films is evidence that a large proportion of existent trap sites are filled up to very near to the conduction band (50 meV) from where they can readily be thermally activated to the conduction band at room temperature, so that the Al_2O_3 -structured perovskite films are effectively n-doped and will have a significantly higher free electron population than the flat films.^{27,38} The increase in dark conductivity, with at least 1 order of magnitude lower mobility, suggests that the effective free electron density in these films will be over 1 order of magnitude higher than in the flat perovskite films.

The origin of the “n-doping” in the mesoporous scaffold is still open. We propose two possible explanations. The first is that under-coordinated iodine ions act as shallow donors at the grain boundaries. Assuming close packed cubes of 60 versus 500 nm width (Figure S4, Supporting Information), we would expect an internal crystal grain boundary area increase of around 10-fold (internal surface area scales as 1/diameter of crystal). Another possibility is that the Al_2O_3 and TiO_2 scaffolds actually help to passivate and even fill traps present at the perovskite surfaces. In fact, the high fixed negative charge density of such metal oxides has been exploited in Si solar cells to passivate surface states, consistent with our observations.^{39,40} The two may even be acting concurrently to induce such a high doping/passivation effect.

In addition to charge-transport photoluminescence, quantum efficiency (PLQE) is an important material property for solar cell applications: every material which absorbs light also has to emit light. However, other nonradiative electron and hole recombination pathways are usually present in addition to this mandatory radiative pathway. Hence, if the solar cell absorber material can be optimized to switch off all the unnecessary recombination pathways, the PLQE will approach 100%.⁴¹ PLQE measurements were performed on both neat flat films and the meso-superstructured films, as has already been done by Deschler *et al.* in recent work.¹² We show in Table 1 that the PLQE measured at room temperature for the solid perovskite films is approximately 20%, which is 1 order of magnitude higher than for the meso-superstructured samples

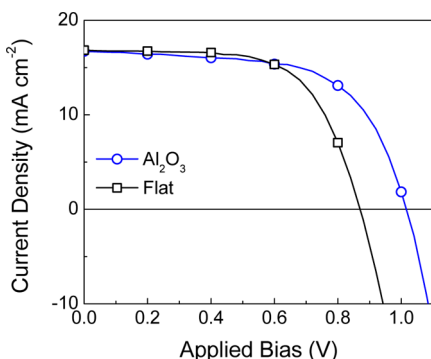


Figure 5. Photocurrent density – voltage (JV) curves of typical planar heterojunction (black circles) and meso-superstructured (blue circles) perovskite solar cells measured under AM1.5 solar simulated light at 100 mW cm^{-2} . These cells were prepared under the same conditions as the samples used for photoconductivity and HAXPES measurements.

at 2%, at a given excitation fluence (see experimental section). This relative behavior is typical for a wide range of excitation densities. Since we generally observe increasing PLQE under increasing excitation densities,¹² the increased doping level in the meso-superstructured film should not by itself result in reduced PLQE. Nonradiative decay occurring through shallow surface states present at the crystal grain boundaries is, however, likely to play a more important role in the meso-superstructured films.

In Figure 5, we present representative current density vs voltage (JV) curves for both planar heterojunction (flat perovskite) and Al_2O_3 -structured (MSSCs) solar cells. We have previously demonstrated that significant improvements in open-circuit voltage and fill factor can be achieved in the planar heterojunction solar cells by obtaining close to 100% perovskite coverage, minimizing leakage current.⁴² However, the open-circuit voltage in the planar heterojunction solar cell is still systematically lower than that of an MSSC. The decrease in photovoltage may be due to the lower doping level. We have already shown by steady-state photoconductivity that charge trapping still dominates at these solar fluences, and far more so for the flat perovskite samples than the MSSCs. We also point out that we have recently demonstrated that the V_{OC} 's of planar heterojunction perovskite solar cells rise at similar time scales as observed for the photoconductivity (Figure 4b) upon illumination at solar fluxes, again attributed to slow sub gap trap filling.¹³ We then conclude that splitting of the quasi-Fermi levels in the perovskite material will be heavily dependent on the

extent to which traps are filled under solar illumination, with a large impact upon the solar cell photovoltage. We also note that vapor-deposited planar heterojunction solar cells based on the same absorber have reached high V_{OC} 's of over 1 V.³ However, the vapor-deposited material is composed of smaller crystals, on the order of a few hundred nanometers in diameter, as compared to the solution-processed solid perovskite layers. If the doping originates from undercoordinated iodine on the crystal surface acting as shallow donors, then it may be that the crystal size in the vapor-deposited films is suitably small to enable sufficient doping. If the origin of traps is due to the presence of impurities or crystal defects, then it is also likely that the evaporative deposition technique, being more readily controlled, minimizes trap formation such that these films can make solar cells with high open circuit voltages.

The high photocurrents obtainable for the MSSCs are also somewhat surprising when one considers that we have observed lower free carrier mobilities and that the PLQE is significantly sub optimum. However, we note that the best performing MSSCs are those where a capping layer of perovskite (50–400 nm) exists on top of the mesostructured layer.^{7,17,18} Ball *et al.* also showed that the IQEs for MSSCs with large capping layers were significantly higher than those without capping layers.⁷ This capping layer will have properties similar to those that we observe for the solid perovskite films; it will be intrinsic and have a high PLQE. Inadvertently, the double layer of meso-structured perovskite film beneath an solid-perovskite capping layer may set up an n–i homojunction, ideal for directional collection of electrons and generating a high voltage. More work is, however, necessary to prove that this is the case.

CONCLUSION

In this work, we demonstrate that although the planar solid perovskite films are superior in radiative efficiency, charge carrier mobilities, and photogenerated species lifetimes, they appear to fall short on open-circuit voltage, likely due to the presence of sub gap trap sites. These are overcome to a certain extent in the MSSC, due to induced doping that fills these traps. Still, the MSSC is a compromise, and in order to reach the full potential of this technology improved understanding and passivation or removal of the sub gap defect sites is required. This will then enable maximum voltages to be achieved in the solid perovskite planar heterojunction solar cells.

MATERIALS AND METHODS

Solar Cells. The synthesis of the perovskite, $\text{CH}_3\text{NH}_3\text{PbI}_{3-x}\text{Cl}_x$, has been reported elsewhere, as has the preparation of the solar cells.¹⁷ Fluorine-doped tin oxide coated glass substrates were cleaned sequentially in Hellmanex, acetone, 2-propanol, and

oxygen plasma. For the MSSCs, a 50 nm compact layer of TiO_2 was deposited by spin coating (2000 rpm, 2000 rpm s⁻¹ ramp) a solution of titanium isopropoxide in ethanol (containing 35 mL of 2 M HCl per 5 mL of solution) and sintered at 500 °C for 30 min. The low-temperature Al_2O_3 scaffold was deposited by spin-coating (speed 2500 rpm, ramp 2500 rpm s⁻¹, time 60 s)

a colloidal dispersion of 50 nm Al_2O_3 nanoparticles (Sigma-Aldrich, product no. 702129) in 2-propanol (1:2 by volume), followed by drying at 150 °C for 10 min, giving a 400 nm scaffold. The perovskite was deposited by spin coating (speed 2000 rpm, ramp 2000 rpm s^{-1} , time 60 s) a 40 wt % DMF solution of methylammonium iodide and PbCl_2 (3:1 molar ratio) in air. The substrate was then heated to 100 °C for 45 min in an oven. For the “flat” cells, the same procedure was followed, but without the Al_2O_3 scaffold deposition. The hole-transport layer was deposited by spin coating an 8.5 vol % 2,20,7,70-tetrakis(*N,N*-bis(*p*-methoxyphenyl)amino)-9,90-spirobifluorene (spiro-MeOTAD) in chlorobenzene solution with the standard additives *tert*-butylpyridine (0.80 mM) and lithium bis(trifluoromethanesulfonyl)imide (20 mM). Gold electrodes were then deposited by evaporation under high vacuum through a shadow mask. For measuring the device performance parameters, solar-simulated AM 1.5 sunlight was generated with an ABET class AAB solar simulator calibrated to give 100 mW cm^{-2} using an NREL-calibrated KG5 filtered silicon reference cell, and the JV curves were recorded with a source meter (Keithley 2400, USA). The solar cells were masked with a metal aperture to define the active area, typically 0.0625 cm^{-2} and measured in a light-tight sample holder to minimize any edge effects. The mismatch factor was calculated to be less than 1% between 400 and 1100 nm.

Conductivity Samples. Here, glass microscope slides were cleaned as described above, and the solar cell preparation was mimicked (for both MSSC and flat configurations) except that no compact TiO_2 layer was used. Gold four-point probe electrodes (50 nm, 6 mm channel length, 10 mm channel width, with two sense electrodes deposited by thermal evaporation inside the channel with 2 mm separation) were then deposited using a shadow mask. As discussed in the main text, some samples were coated with a 10 vol % solution of spiro-MeOTAD in chlorobenzene in the absence of any additives, while others were coated by a solution of 20 mg mL^{-1} of poly(methyl methacrylate) (PMMA), all spin coated for 60 s at 2000 rpm with a 2000 rpm s^{-1} ramp rate.

Photoluminescence Studies. Photoluminescence quantum efficiency (PLQE) measurements were taken in an integrating sphere using established techniques.⁴³ The samples were photoexcited using a 532 nm CW laser operating at a fluence of 1600 mW/cm². The signals were collected using a fiber-coupled Ocean Optics 2000+ spectrometer.

HAXPES. The hard X-ray photoelectron spectroscopy (HAXPES) measurements at high kinetic energy (approximately 4 keV) were performed using hard X-ray synchrotron light at the high kinetic energy electron spectroscopy (HKE) end station on the beamline KMC-1 at BESSY in Berlin.⁴⁴ The spectra were energy calibrated using a gold foil and setting the Fermi-level to 0 eV binding energy.

Conductivity Measurements in the Dark. Voltage was applied to the outer electrodes, and the current flowing through them was monitored by a Keithley sourcemeter. The potential across electrodes inner electrodes was monitored, allowing us to accurately determine the potential between the outer electrodes, regardless of the contact resistance.

Photoconductivity. A continuous diode laser was used at the range of fluences specified in the main text, with an excitation wavelength of 473 nm and a modulation frequency of 123 Hz. A bias of 25 V was applied across the outer electrodes, while the current was monitored by an oscilloscope, as described in detail elsewhere.^{27,45} The resistance through the oscilloscope was set by a variable resistor to always be <1% of the sample resistance. We monitored the voltage between the inner probes (separation 1/3 of the channel length) of the four-point probe electrode pattern through a 1 G Ω impedance Autolabs potentiostat to determine the potential dropped across the total channel length. We then confirmed this by doing full IV curves of the samples at various light intensities, as shown in the Supporting Information. Transient photoconductivity was taken on an oscilloscope, as described for the steady-state photoconductivity, but now the excitation source was an Nd:YAG laser tuned to 500 nm, pumped at 10 Hz with 7 ns pulses.

Cyclic Voltammetry. Cyclic voltammetry measurements were carried out on perovskite films on FTO with and without an Al_2O_3 scaffold, as described in the Solar Cells section.

The electrolyte was 0.03 M $\text{Et}_4\text{N TFSI}$ in chlorobenzene, and the solution was purged with nitrogen prior to taking any measurements to ensure that no oxygen was present. Measurements were carried out in a three-electrode configuration, with Pt wire as a counter electrode and Ag wire acting as a pseudoreference electrode. The potential was controlled *via* a potentiostat (Versastat 3, Princeton Applied Research) using the VersaStudio Software.

Conflict of Interest: The authors declare no competing financial interest.

Acknowledgment. We thank J. Oscarsson and B. Philippe for help in performing the HAXPES measurements. We thank Dr. A. Petrozza, Dr. G. Grancini, Dr. A. Kandada, and Dr. V. M. Burlakov for valuable discussions. The research leading to these results has received funding from the European Union Seventh Framework Program (FP7/2007-2013) under Grant Agreement 316494.

Supporting Information Available: Figures S1–S4 and discussion as described in the text. This material is available free of charge *via* the Internet at <http://pubs.acs.org>.

REFERENCES AND NOTES

- Lee, M. M.; Teuscher, J.; Miyasaka, T.; Murakami, T. N.; Snaith, H. J. Efficient Hybrid Solar Cells Based on Mesosuperstructured Organometal Halide Perovskites. *Science* (80-). **2012**, *338*, 643–647.
- Kim, H.-S.; Lee, C.-R.; Im, J.-H.; Lee, K.-B.; Moehl, T.; Marchioro, A.; Moon, S.-J.; Humphry-Baker, R.; Yum, J.-H.; Moser, J. E.; et al. Lead Iodide Perovskite Sensitized All-Solid-State Submicron Thin Film Mesoscopic Solar Cell with Efficiency Exceeding 9%. *Sci. Rep.* **2012**, *2*.
- Liu, M.; Johnston, M. B.; Snaith, H. J. Efficient Planar Heterojunction Perovskite Solar Cells by Vapour Deposition. *Nature* **2013**, *501*, 395–398.
- Burschka, J.; Pellet, N.; Moon, S.-J.; Humphry-Baker, R.; Gao, P.; Nazeeruddin, M. K.; Grätzel, M. Sequential Deposition as a Route to High-Performance Perovskite-Sensitized Solar Cells. *Nature* **2013**, *499*, 316–319.
- Etgar, L.; Gao, P.; Xue, Z.; Peng, Q.; Chandiran, A. K.; Liu, B.; Nazeeruddin, M. K.; Grätzel, M. Mesoscopic $\text{CH}_3\text{NH}_3\text{PbI}_3/\text{TiO}_2$ Heterojunction Solar Cells. *J. Am. Chem. Soc.* **2012**, *134*, 17396–17399.
- Laban, W. A.; Etgar, L. Depleted Hole Conductor-Free Lead Halide Iodide Heterojunction Solar Cells. *Energy Environ. Sci.* **2013**, *6*, 3249–3253.
- Ball, J. M.; Lee, M. M.; Hey, A.; Snaith, H. J. Low-Temperature Processed Meso-Superstructured to Thin-Film Perovskite Solar Cells. *Energy Environ. Sci.* **2013**, *6*, 1739–1743.
- Stranks, S. D.; Eperon, G. E.; Grancini, G.; Menelaou, C.; Alcocer, M. J. P.; Leijtens, T.; Herz, L. M.; Petrozza, A.; Snaith, H. J. Electron-Hole Diffusion Lengths Exceeding 1 Micrometer in an Organometal Trihalide Perovskite Absorber. *Science* **2013**, *342*, 341–344.
- Xing, G.; Mathews, N.; Sun, S.; Lim, S. S.; Lam, Y. M.; Grätzel, M.; Mhaisalkar, S.; Sum, T. C. Long-Range Balanced Electron- and Hole-Transport Lengths in Organic-Inorganic $\text{CH}_3\text{NH}_3\text{PbI}_3$. *Science* **2013**, *342*, 344–347.
- Edri, E.; Kirmayer, S.; Henning, A.; Mukhopadhyay, S.; Gartsman, K.; Rosenwaks, Y.; Hodes, G.; Cahen, D. Why Lead Methylammonium Tri-IODIDE Perovskite-Based Solar Cells Require a Mesoporous Electron Transporting Scaffold (but Not Necessarily a Hole Conductor). *Nano Lett.* **2014**, *14*, 1–18.
- Wehrenfennig, C.; Eperon, G. E.; Johnston, M. B.; Snaith, H. J.; Herz, L. M. High Charge Carrier Mobilities and Lifetimes in Organolead Trihalide Perovskites. *Adv. Mater.* **2013**, *26*, 1584–1589.
- Deschler, F.; Price, M.; Pathak, S.; Klintberg, L. E.; Jarausch, D.-D.; Higler, R.; Hüttner, S.; Leijtens, T.; Stranks, S. D.; Snaith, H. J.; et al. High Photoluminescence Efficiency and Optically Pumped Lasing in Solution-Processed Mixed Halide Perovskite Semiconductors. *J. Phys. Chem. Lett.* **2014**, *14*, 1421–1426.

13. Stranks, S. D.; Burlakov, V. M.; Leijtens, T.; Ball, J. M.; Goriely, A.; Snaith, H. J. Photoluminescence from Organometal Halide Perovskites: Excitons, Free Charge and Sub-Gap Electronic States, submitted for publication.
14. Docampo, P.; Ball, J. M.; Darwich, M.; Eperon, G. E.; Snaith, H. J. Efficient Organometal Trihalide Perovskite Planar-Heterojunction Solar Cells on Flexible Polymer Substrates. *Nat. Commun.* **2013**, *4*, 2761.
15. Malinkiewicz, O.; Yella, A.; Lee, Y. H.; Espallargas, G. M.; Graetzel, M.; Nazeeruddin, M. K.; Bolink, H. J. Perovskite Solar Cells Employing Organic Charge-Transport Layers. *Nat. Photonics* **2013**, *8*, 1–5.
16. Liu, D.; Kelly, T. L. Perovskite Solar Cells with a Planar Heterojunction Structure Prepared Using Room-Temperature Solution Processing Techniques. *Nat. Photonics* **2013**, *8*, 1–6.
17. Wang, J. T.-W.; Ball, J. M.; Barea, E. M.; Abate, A.; Alexander-Webber, J. a.; Huang, J.; Saliba, M.; Mora-Sero, I.; Bisquert, J.; Snaith, H. J.; et al. Low-Temperature Processed Electron Collection Layers of Graphene/TiO₂ Nanocomposites in Thin Film Perovskite Solar Cells. *Nano Lett.* **2013**, *14*, 724–730.
18. Wojciechowski, K.; Saliba, M.; Leijtens, T.; Abate, A.; Snaith, H. Supporting Information: Sub 150 °C Processed Meso-Superstructured Perovskite Solar Cells with Enhanced Efficiency. *Energy Environ. Sci.* **2013**, *2*, 1–5.
19. Eperon, G. E.; Burlakov, V. M.; Docampo, P.; Goriely, A.; Snaith, H. J. Morphological Control for High Performance, Solution-Processed Planar Heterojunction Perovskite Solar Cells. *Adv. Funct. Mater.* **2013**, *24*, 151–157.
20. You, J.; Hong, Z.; Yang, Y. M.; Chen, Q.; Cai, M.; Song, T.; Chen, C.; Lu, S.; Liu, Y.; Zhou, H.; et al. Perovskite Solar Cells with High Efficiency and Flexibility **2014**, *7*, 994–997.
21. Lindblad, R.; Bi, D.; Park, B.; Oscarsson, J.; Gorgoi, M.; Siegbahn, H.; Odelius, M.; Johansson, E. M. J.; Rensmo, H. The Electronic Structure of TiO₂/CH₃NH₃PbI₃ Perovskite Solar Cell Interfaces. *J. Phys. Chem. Lett.* **2014**, *5*, 648–653.
22. Kim, H.-S.; Mora-Sero, I.; Gonzalez-Pedro, V.; Fabregat-Santiago, F.; Juarez-Perez, E. J.; Park, N.-G.; Bisquert, J. Mechanism of Carrier Accumulation in Perovskite Thin-Absorber Solar Cells. *Nat. Commun.* **2013**, *4*, 2242.
23. Yin, W.-J.; Shi, T.; Yan, Y. Unusual Defect Physics in CH₃NH₃PbI₃ Perovskite Solar Cell Absorber. *Appl. Phys. Lett.* **2014**, *104*, 063903.
24. Shkrob, I. A.; Marin, T. W. Charge Trapping in Photovoltaically Active Perovskites and Related Halogenoplumbate Compounds. *J. Phys. Chem. Lett.* **2014**, *5*, 1066–1071.
25. Bertoluzzi, L.; Badia-Bou, L.; Fabregat-Santiago, F.; Gimenez, S.; Bisquert, J. Interpretation of Cyclic Voltammetry Measurements of Thin Semiconductor Films for Solar Fuel Applications. *J. Phys. Chem. Lett.* **2013**, *4*, 1334–1339.
26. Snaith, H. J.; Grätzel, M. Electron and Hole Transport through Mesoporous TiO₂ Infiltrated with Spiro-MeOTAD. *Adv. Mater.* **2007**, *19*, 3643–3647.
27. Leijtens, T.; Lim, J.; Teuscher, J.; Park, T.; Snaith, H. J. Charge Density Dependent Mobility of Organic Hole-Transporters and Mesoporous TiO₂ Determined by Transient Mobility Spectroscopy: Implications to Dye-Sensitized and Organic Solar Cells. *Adv. Mater.* **2013**, *25*, 3227–3233.
28. D'Innocenzo, V.; Grancini, G.; Alcocer, M. J. P.; Kandada, A. R. S.; Stranks, S. D.; Lee, M. M.; Lanzani, G.; Snaith, H. J.; Petrozza, A. Excitons versus Free Charges in Organo-Lead Tri-Halide Perovskites. *Nat. Commun.* **2014**, *5*, 3586.
29. Marchioro, A.; Teuscher, J.; Friedrich, D.; Kunst, M.; van de Krol, R.; Moehl, T.; Grätzel, M.; Moser, J.-E. Unravelling the Mechanism of Photoinduced Charge Transfer Processes in Lead Iodide Perovskite Solar Cells. *Nat. Photonics* **2014**, *1*–6.
30. Ponseca, C. S.; Savenije, T. J.; Abdellah, M.; Zheng, K.; Yartsev, A.; Pascher, T.; Harlang, T.; Chabera, P.; Pullerits, T.; Stepanov, A.; et al. Organometal Halide Perovskite Solar Cell Materials Rationalized: Ultrafast Charge Generation, High and Microsecond-Long Balanced Mobilities, and Slow Recombination. *J. Am. Chem. Soc.* **2014**, *136*, 5189–5192.
31. Tanaka, K.; Takahashi, T.; Ban, T.; Kondo, T.; Uchida, K.; Miura, N. Comparative Study on the Excitons in Lead-Halide-Based Perovskite-Type Crystals CH₃NH₃PbBr₃ CH₃NH₃PbI₃. *Solid State Commun.* **2003**, *127*, 619–623.
32. Giorgi, G.; Fujisawa, J.-I.; Segawa, H.; Yamashita, K. Small Photocarrier Effective Masses Featuring Ambipolar Transport in Methylammonium Lead Iodide Perovskite: A Density Functional Analysis. *J. Phys. Chem. Lett.* **2013**, *4*, 4213–4216.
33. Stoumpos, C. C.; Malliakas, C. D.; Kanatzidis, M. G. Semiconducting Tin and Lead Iodide Perovskites with Organic Cations: Phase Transitions, High Mobilities, and Near-Infrared Photoluminescent Properties. *Inorg. Chem.* **2013**, *52*, 9019–9038.
34. Holliday, S.; Donaghey, J. E.; McCulloch, I. Advances in Charge Carrier Mobilities of Semiconducting Polymers Used in Organic Transistors. *Chem. Mater.* **2013**, *26*, 647–663.
35. Fortunato, E.; Barquinha, P.; Martins, R. Oxide Semiconductor Thin-Film Transistors: A Review of Recent Advances. *Adv. Mater.* **2012**, *24*, 2945–2986.
36. Tiwana, P.; Docampo, P.; Johnston, M. B.; Snaith, H. J.; Herz, L. M. Electron Mobility and Injection Dynamics in Mesoporous ZnO, SnO₂, and TiO₂ Films Used in Dye-Sensitized Solar Cells. *ACS Nano* **2011**, *5*, 5158–5166.
37. Edri, E.; Kirmayer, S.; Mukhopadhyay, S.; Gartsman, K.; Hodes, G.; Cahen, D. Elucidating the Charge Carrier Separation and Working Mechanism of CH₃NH₃PbI₃–xClx Perovskite Solar Cells. *Nat. Commun.* **2014**, *5*, 3461.
38. Shuttle, C. G.; Hamilton, R.; Nelson, J.; O'Regan, B. C.; Durrant, J. R. Measurement of Charge-Density Dependence of Carrier Mobility in an Organic Semiconductor Blend. *Adv. Funct. Mater.* **2010**, *20*, 698–702.
39. Aberle, A. G. Surface Passivation of Crystalline Silicon Solar Cells: A Review. *Prog. Photovoltaics Res. Appl.* **2000**, *8*, 473–487.
40. Hezel, R.; Jaeger, K. Low-Temperature Surface Passivation of Silicon for Solar Cells. *J. Electrochem. Soc.* **1989**, *136*, 518.
41. Miller, O. D.; Yablonovitch, E.; Kurtz, S. R. Strong Internal and External Luminescence as Solar Cells Approach the Shockley & Queisser Limit. *Photovoltaics, IEEE J.* **2012**, *2*, 303–311.
42. Eperon, G. E.; Burlakov, V. M.; Docampo, P.; Goriely, A.; Snaith, H. J. Morphological Control for High Performance, Solution-Processed Planar Heterojunction Perovskite Solar Cells. *Adv. Funct. Mater.* **2013**, *24*, 151–157.
43. deMello, J. C.; Wittmann, H. F.; Friend, R. H. An Improved Experimental Determination of External Photoluminescence Quantum Efficiency. *Adv. Mater.* **1997**, *9*, 230–232.
44. Gorgoi, M.; Svensson, S.; Schäfers, F.; Öhrwall, G.; Mertin, M.; Bressler, P.; Karis, O.; Siegbahn, H.; Sandell, A.; Rensmo, H.; et al. The High Kinetic Energy Photoelectron Spectroscopy Facility at BESSY Progress and First Results. *Nucl. Instruments Methods Phys. Res. Sect. A Accel. Spectrometers, Detect. Assoc. Equip.* **2009**, *601*, 48–53.
45. Petrozza, A.; Groves, C.; Snaith, H. J. Electron Transport and Recombination in Dye-Sensitized Mesoporous TiO₂ Probed by Photoinduced Charge-Conductivity Modulation Spectroscopy with Monte Carlo Modeling. *J. Am. Chem. Soc.* **2008**, *130*, 12912–12920.